

Development of a Photoswitchable Lithium-Sensitive Probe to Analyze Nonselective Cation Channel Activity in Migrating Cancer Cells

Jinxin V. Pei, Sabrina Heng, Michael L. De Ieso, Georgina Sylvia, Mohamad Kourghi, Saeed Nourmohammadi, Andrew D. Abell, and  Andrea J. Yool

Adelaide Medical School, and the Institute for Photonics and Advanced Sensing (IPAS) (J.V.P., M.D.I., M.K., S.N., A.J.Y.) and ARC Centre of Excellence for Nanoscale BioPhotonics, IPAS, School of Physical Sciences (S.H., G.S., A.D.A.), University of Adelaide, Adelaide, South Australia, Australia

Received December 3, 2018; accepted March 5, 2019

ABSTRACT

This is the first work to use a newly designed Li⁺-selective photoswitchable probe Sabrina Heng Lithium (SHL) in living colon cancer cells to noninvasively monitor cation channel activity in real time by the appearance of lithium hot spots detected by confocal microscopy. Punctate Li⁺ hot spots are clustered in the lamellipodial leading edges of HT29 human colon cancer cells and are colocalized with aquaporin-1 (AQP1) channels. AQP1 is a dual water and cyclic-nucleotide-gated cation channel located in lamellipodia and is essential for rapid cell migration in a subset of aggressive cancers. Both the Li⁺ hot spots and cell migration are blocked in HT29 cells by the AQP1 ion channel antagonist AqB011. In contrast, Li⁺ hot spots are not evident in a poorly migrating colon cancer cell line, SW620, which lacks comparable membrane expression of

AQP1. Knockdown of AQP1 by RNA interference in HT29 cells significantly impairs Li⁺ hot spot activity. The SHL probe loaded in living cells shows signature chemical properties of ionic selectivity and reversibility. Dynamic properties of the Li⁺ hot spots, turning on and off, are confirmed by time-lapse imaging. SHL is a powerful tool for evaluating cation channel function in living cells in real time, with particular promise for studies of motile cells or interlinked networks not easily analyzed by electrophysiological methods. The ability to reset SHL by photoswitching allows monitoring of dynamic signals over time. Future applications of the Li⁺ probe could include high-throughput optical screening for discovering new classes of channels, or finding new pharmacological modulators for nonselective cation channels.

Introduction

Cell migration is central to critical processes of repair, regeneration, immune protection, development, and maintenance of multicellular organisms, and in disease conditions such as cancer metastasis (Friedl and Wolf, 2003; Papadopoulos et al., 2008; Olson and Sahai, 2009; Petrie et al., 2009; Krummel et al., 2016). In addition to regulating fluid balance (Agre et al., 1993; King et al., 2004), some aquaporins facilitate rapid cell migration. For example, aquaporin-1 (AQP1) enhances the mobility of some of the most motile cells, such as T cells,

fibroblasts, cancers, and amoebae (Pei et al., 2016a). While the exact mechanisms have yet to be determined, we do know that elevated expression of AQP1 is apparent at the leading edges of lamellipodia in these classes of migrating cells. Genetic knockdown of AQP1 expression can impair cell migration significantly (Hu and Verkman, 2006; McCoy and Sontheimer, 2007), whereas reintroduction of AQP1 but not other channels, such as AQP4, can restore motility (McCoy and Sontheimer, 2007). A major difference is that AQP1, but not AQP4, can function as a nonselective monovalent cation channel gated by cGMP, as well as a water channel (Anthony et al., 2000; Boassa and Yool, 2003). Dissecting the role of AQP1 ion channels in cell migration would advance our knowledge of basic mechanisms that enhance motility in cancer, stem cells, and regenerating tissues, and identify possible targets for intervention, such as in cancer metastasis.

Here, we demonstrate that a newly designed reversible lithium sensor Sabrina Heng Lithium (SHL) can be used to monitor cation channel activity in living cells, and we demonstrate proof of principle using a metastatic colon cancer cell line (HT29) that relies on high levels of AQP1 expression for rapid migration capability (Dorward et al., 2016) as compared with a

This work was supported by the Australian Research Council [Grants DP160104641 and DP190101745]. Sensor development was supported by the Centre for Nanoscale BioPhotonics, with funding from the Australian Research Council [Grant CE140100003].

Part of this work was presented at the 2018 Biophysics Conference, and the abstract was published in the following Biophysical Journal conference proceedings: Pei JV, Heng S, De Ieso M, Sylvia G, Kourghi M, Abell AD, and Yool AJ (2018) Real-Time Imaging of Lithium 'Hot-Spots': An Analysis of Ion Conductance in Aquaporin-1 using Novel Photo-Switchable Sensor. *Biophys J* 114:360a DOI: 10.1016/j.bpj.2017.11.1999.

<https://doi.org/10.1124/mol.118.115428>.

 This article has supplemental material available at molpharm.aspetjournals.org.

ABBREVIATIONS: AQP1, aquaporin-1; DMEM, Dulbecco's modified Eagle's medium; Em, emission; Ex, excitation; MC, merocyanine; PBS, phosphate-buffered saline; PCR, polymerase chain reaction; RFU, relative fluorescence unit; RT, room temperature; SHL, Sabrina Heng Lithium; siRNA, small interfering RNA; SP, spiropyran; TEA, tetraethylammonium.

relatively sedentary colon cancer line (SW620), which lacks high AQP1 expression (Smith et al., 2018). SHL was designed to be selective for a low-abundance monovalent ion, Li^+ , over Na^+ and K^+ . AQP1 ion channels have properties that make them an excellent choice for this study; once activated, they show long open times (with open bursts lasting hundreds of milliseconds), a high single-channel conductance (150 pS in physiologic salines), and high permeability to monovalent cations Na^+ , K^+ , and Cs^+ (Anthony et al., 2000). Work here shows the AQP1 ion channel is also permeable to Li^+ and, thus, can be hypothesized to enable Li^+ ion influx, which could be detected by the SHL probe. The exciting finding that launched this study was the observation that the punctate SHL signals are clustered in the lamellipodia of migrating cancer cells. Subsequent confirmation that SHL detects AQP1-mediated Li^+ entry took advantage of the selective AQP1 ion channel inhibitor (AqB011), cation-substituted extracellular salines, and molecular knockdown of AQP1 to show that Li^+ entry into the cells and the punctate hot spot signals depended on the presence of ion-conducting AQP1 channels.

Results here show that activation of the sensor intracellularly is dependent on transport of extracellular Li^+ into the cell. Since the SHL probe is membrane-permeable, it is expected to be uniformly distributed through the cell; the presence of discrete points of fluorescent signal (“hot spots”) implies locations of increased lithium entry. Selective inhibition of AQP1 with AqB011 and knockdown of AQP1 with small interfering RNA show that the Li^+ transport occurs through AQP1 channels. These results provide the first evidence of hot spots that colocalize with nonselective monovalent cation channels, as confirmed by properties of pharmacological sensitivity, ion selectivity, and levels of expression. These data illustrate the selectivity and applicability of the SHL probe as a powerful biologic tool and add further support to the idea that the ion channel function of AQP1 is an intriguing target for new strategies to manage AQP1-expressing cancers.

Materials and Methods

Oocyte Expression and Electrophysiology. Two electrode voltage clamp recordings were used to determine the ability of Li^+ to carry current in AQP1-expressing oocytes. Oocyte preparation and cRNA injection were performed as detailed in previous studies (Kourghi et al., 2016; Pei et al., 2016b). In brief, with a protocol approved by the University of Adelaide Animal Ethics Committee (M2018-016) in accord with Australian National Guidelines, partial ovariectomy of anesthetized adult *Xenopus laevis* female frogs was used to obtain lobes of unfertilized oocytes. Oocytes were separated from follicular coats with collagenase, rinsed in Ca^{2+} -free isotonic Na^+ saline, and incubated in frog Ringer’s saline at 16–18°C. Selected oocytes were injected with 30–50 nl of sterile water with and without 1 ng of cRNA from cloned human Aquaporin-1 (NM_198098), linearized, and transcribed in vitro as per published methods. Oocytes without AQP1 cRNA served as non-AQP-expressing controls. Recordings were performed at room temperature in standard isotonic Na^+ saline or in Li^+ -substituted isotonic saline containing either 100 mM NaCl or 100 mM LiCl, and 2 mM KCl, 4.5 mM MgCl_2 , and 5 mM HEPES, pH 7.3. Capillary glass electrodes (1–3 M Ω ; 1 M KCl) were used for recordings. cGMP was applied to the bath saline at a final concentration of 10–20 μM using the membrane-permeable cGMP analog [Rp]-8-[para-chlorophenylthio]-cGMP (Sigma-Aldrich, Castle Hill, NSW, Australia). Ion conductances were determined by linear fits of current amplitudes as a function of voltage, applied by a step protocol from +60 to –110 mV from a –40-mV holding

potential (Kourghi et al., 2016; Pei et al., 2016b). Ionic conductance values were monitored over 25 minutes after the bath application of cGMP to allow sufficient time to achieve maximal response. Recordings were done using a GeneClamp amplifier and pClamp 9.0 software (Molecular Devices, Sunnyvale, CA).

Cancer Cell Cultures and Confocal Imaging. HT29 and SW620 colorectal cancer cell lines (American Type Culture Collection, Manassas, VA) were cultured in Dulbecco’s modified Eagle’s medium (DMEM) supplemented with 10% fetal bovine serum (v/v), penicillin and streptomycin (100 U/ml each), and 1 \times glutamax (Life Technologies, Scoresby, VIC, Australia), referred to as complete DMEM. Cultures were maintained in 5% CO_2 at 37°C. Cells were seeded on eight-well uncoated Ibidi μ -Slides (Ibidi, Munich, Germany) at a density of 1.0×10^5 cells/ml and allowed 24 hours to settle.

All imaging experiments were performed in a darkroom. Prior to imaging, cells were incubated with 50 μM SHL sensor for 2 hours, then washed twice with warm phosphate-buffered saline. For the AqB011-treated group, cells were then incubated with 20 to 80 μM AqB011 for 2 hours or with vehicle (0.1% dimethylsulfoxide). All cells were stained with 0.5 mg/ml of Hoechst 33258 for 20 minutes. Either Li^+ saline (137 mM LiCl, 3.5 mM KCl, 0.68 mM KH_2PO_4 , 5 mM HEPES, 10 mM glucose, and 4.4 mM MgSO_4) or tetraethylammonium (TEA^+) saline (with 137 mM TEA Cl substituted for LiCl and all other components identical to those in Li^+ saline) was used for the imaging. The μ -Slide was mounted on a Leica TCS SP5 laser-scanning confocal microscope (Leica, Wetzlar, Germany) with the 63 \times objective selected. To detect the signal emitted by the SHL sensor, the following excitation (Ex)/emission (Em) setting was used: Ex = 513 nm/Em = 550 nm–700 nm. For visualizing Hoechst 33258 staining, the following setting was used: Ex = 405 nm/Em = 425–500 nm.

Small Interfering RNA Transfection. HT29 cells were cultured in six-well plates or eight-well uncoated Ibidi μ -Slides in complete DMEM medium to reach 30% confluency prior to transfection. Transfection with Lipofectamine 2000 (11668019; Life Technologies) used 50 nM of either Ambion Silencer Select AQP1 siRNA (4390824; Life Technologies) or Ambion Silencer Select Negative Control #1 siRNA (4390843; Life Technologies), together with 50 nM Dharmacon siGLO Green Transfection Indicator (D-001630-01-05; Millennium Science, Mulgrave, VIC, Australia). Cells were incubated in 5% CO_2 at 37°C for 48 hours prior to confocal imaging or real-time polymerase chain reaction (PCR) analyses. For signals emitted by siGLO Green, the setting Ex = 496 nm/Em = 506 nm–606 nm was used.

Quantitative Reverse-Transcription Polymerase Chain Reaction. At 48 hours post-transfection, cells were harvested from six-well plates, and RNA was extracted using Invitrogen PureLink RNA Mini Kit (1876897; Life Technologies) according to the manufacturer’s protocol. RNA was quantified in Take3 Micro-Volume Plates with a Synergy 2 plate reader (BioTek, Winooski, VT). RNA (1 μg) was reverse transcribed using the QuantiNOVA Reverse Transcription kit (205413; Qiagen, Chadstone Centre, VIC, Australia). Quantitative reverse-transcription polymerase chain reactions of the reference sequence ribosomal protein S13 (RPS13) and AQP1 were performed using SYBR Select Master Mix (4472908; Life Technologies) in triplicate using the Rotorgene 6000 (Qiagen). Primers used for AQP1 were as follows: forward primer, AGTCACTTCCCAAGATCTGC; reverse primer, CAGGTGGGTCCCTTTCTTTCA.

Immunohistochemistry. Cells were cultured in eight-well Ibidi μ -Slides to achieve 50% confluency prior to the experiment. Cells were rinsed with phosphate-buffered saline (PBS), fixed in 4% paraformaldehyde for 20 minutes at room temperature (RT), and washed four times in PBS (5-minute washes at RT) on a rocker. Cells were permeabilized with 0.1% PBS Tween for 5 minutes, washed three times with PBS at RT for 5 minutes on a rocker, and then blocked with 10% goat serum in PBS (GS/PBS) for 40 minutes at RT on a rocker. Incubation with the rabbit anti-AQP1 antibody (ab15080; Abcam, VIC, Australia) in 0.1% GS/PBS lasted 2 hours at RT. The cells were then washed three times in PBS (7 minutes; RT) on a rocker and incubated with AlexaFluor 488-conjugated goat anti-rabbit antibody

(ab150077; Abcam) diluted in 0.1% GS/PBS (35 minutes; RT, in the dark). After washing three times in PBS (7 minutes; RT) on a rocker, cells were incubated with Hoechst 33258 (Sigma-Aldrich) for 5 minutes in the dark. The cells were rinsed with PBS twice and mounted using Hydromount mounting medium (Sigma-Aldrich).

In Cell Photoswitching Experiment. The plate was mounted on a microscope with an overhanging UV lamp and table light. The first image was taken after the plate had been exposed to white light for 10 minutes (OFF1). The second image was taken after subsequent UV (632 nm) light exposure for 10 minutes (ON1). Over the next 10 minutes, images were captured every 2 minutes during white light exposure, ending with the seventh image (OFF2). The final image was taken after 10-minute incubation in total darkness (ON2). Fluorescent intensities were quantified using ImageJ software (National Institutes of Health, Bethesda, MD).

Chemical Synthesis and Characterization. Details for the synthesis of SHL are reported as Supplemental Materials (Supplemental Synthesis Experiment and Supplemental Scheme 1). The characterization of SHL is provided as Supplemental Materials (Supplemental Spectroscopic Experiments), which show the absorbance spectrum (Supplemental Fig. 1), Job's plot analysis of binding stoichiometry (Supplemental Fig. 2), photoswitching properties (Supplemental Fig. 3), metal ion titration tests (Supplemental Fig. 4), and results for excitation to emission to absorbance integration (Supplemental Fig. 5).

Statistics. Differences were analyzed for significance using one-way analysis of variance for multiple comparisons where relevant and post hoc analyses by Student's unpaired *t* test unless otherwise indicated.

Results are reported as $P < 0.001$ (***) and $P < 0.0001$ (****); *n* values are indicated above the *x*-axis (*n*) in histograms.

Results

Design and Characterization of the Reversible Lithium Sensor SHL. The sensor described here (see Fig. 1A for SHL structure) contains a photochromic spiropyran that can be reversibly switched between a nonfluorescent spiropyran isomer (SP) and a charge-delocalized fluorescent merocyanine isomer (MC) when interacting with an appropriate metal ion (Rivera-Fuentes et al., 2015), such as Li^+ (Fig. 1A). The ability to switch between the two states is advantageous for visualizing Li^+ transport into cells. SHL shows enhanced fluorescence when complexed to Li^+ (MC- Li^+ complex in Fig. 1A) while maintaining low background fluorescence in the absence of the ion (SP isomer in Fig. 1A). This sensor characteristic is desirable for visualizing ion binding with confocal microscopy and is predicted to yield better resolution than conventional fluorescent probes due to its enhanced signal-to-background ratio (Kolmakov et al., 2010; Klajn, 2014). A critical characteristic of the SHL sensor is its selectivity for Li^+ over other biologically abundant ions. We showed that incorporation of suitable ionophores on the spiropyran nucleus provided selective binding of defined ions (Heng et al., 2017). Here, we incorporated a 1-aza-15-crown-5 substituent at

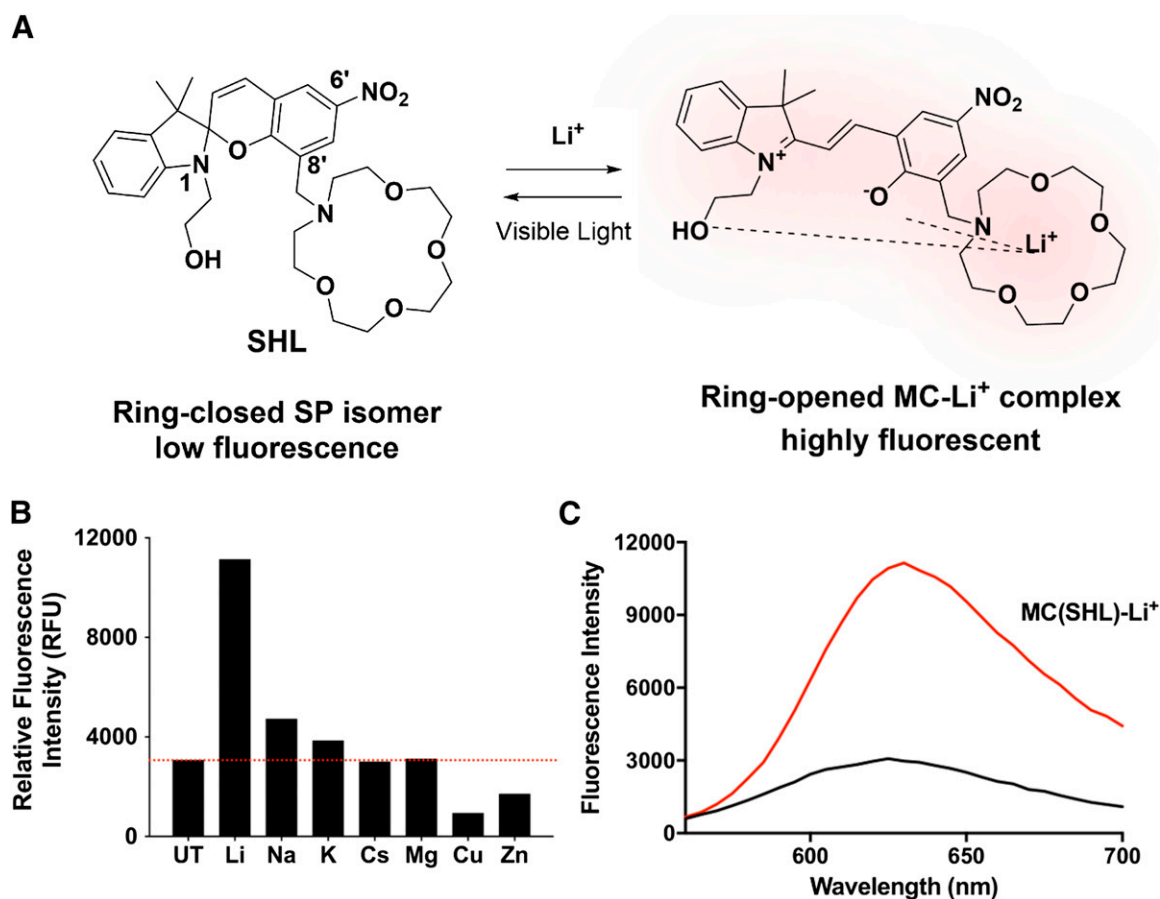


Fig. 1. Properties of the lithium sensor SHL. (A) Structures of the SP and merocyanine-lithium complexes of the sensor SHL [MC(SHL)- Li^+] and reversible binding of Li^+ . The ring-closed spiropyran has lower fluorescence than the open merocyanine. (B) Fluorescence intensities of SHL (50 μM) in the presence of Li^+ or other biologically relevant metal ions. Excitation wavelength = 532 nm; emission wavelength = 625 nm. (C) Fluorescence spectra of SHL in water (50 μM). Black spectrum, SHL with no added Li^+ ; red spectrum, SHL with Li^+ (100 μM).

C8 and a hydroxyethyl substituent at N1 to impart selectivity for Li^+ (Fig. 1A). Finally, we incorporated an NO_2 substituent at C6 of the benzopyran ring as an electron-withdrawing group at that position, known to stabilize the ring-opened MC form, thus favoring ion binding. Details on the synthesis of SHL are reported in the synthesis section of the Supplemental Information. In brief, the Li^+ sensor was prepared from 1-aza-15-crown-5 and 1-(2-hydroxyethyl)-2,3,3-trimethyl-3H-indol-1-ium to give SHL with an overall yield of 20% using a modification to existing methodology (Heng et al., 2013; Stubing et al., 2016).

The addition of excess Li^+ (100 μM) to SHL (50 μM) gave rise to strong fluorescence ($\lambda_{\text{ex}} = 532 \text{ nm}$) at approximately $\lambda_{\text{em}} = 635 \text{ nm}$, as shown in Fig. 1C, which is consistent with the formation of the MC(SHL)- Li^+ complex as expected based on our sensor design. Importantly, the red fluorescence represents an emission bandwidth that is distinct from the blue nuclear stain (Hoechst 33258) and green AQP1 immunofluorescence signals. Additional spectroscopic properties of SHL, such as absorbance, detection limits, photoswitching, and

quantum yields, are detailed in the Supplemental Note section. The selectivity of SHL for Li^+ over other biologically relevant ions was confirmed through ion binding assays with the addition of excess ions (Li^+ , Na^+ , K^+ , Cs^+ , Mg^{2+} , Mn^{2+} , Cu^{2+} , or Zn^{2+}). Results in Fig. 1B show that SHL had the highest affinity for Li^+ and relatively little response to similar monovalent ions, such as Na^+ and K^+ . The red-emitting properties and selectivity of SHL for Li^+ demonstrated that the emission observed in the cell was not due to autofluorescence or interaction of the sensor with other endogenous ions; the signal was specific to the MC(SHL)- Li^+ complex.

The AQP1 Cation Channel Is Permeable to Li^+ and Blocked by AqB011. AQP1-expressing and non-AQP control *Xenopus* oocytes were recorded by two-electrode voltage clamp in isotonic saline with 137 mM Li^+ substituted for standard physiologic Na^+ . Ion currents in isotonic Li^+ saline (Fig. 2A) were measured for human AQP1-expressing *Xenopus* oocytes and nonexpressing control oocytes before (“initial”) and after treatment with a membrane-permeable analog of

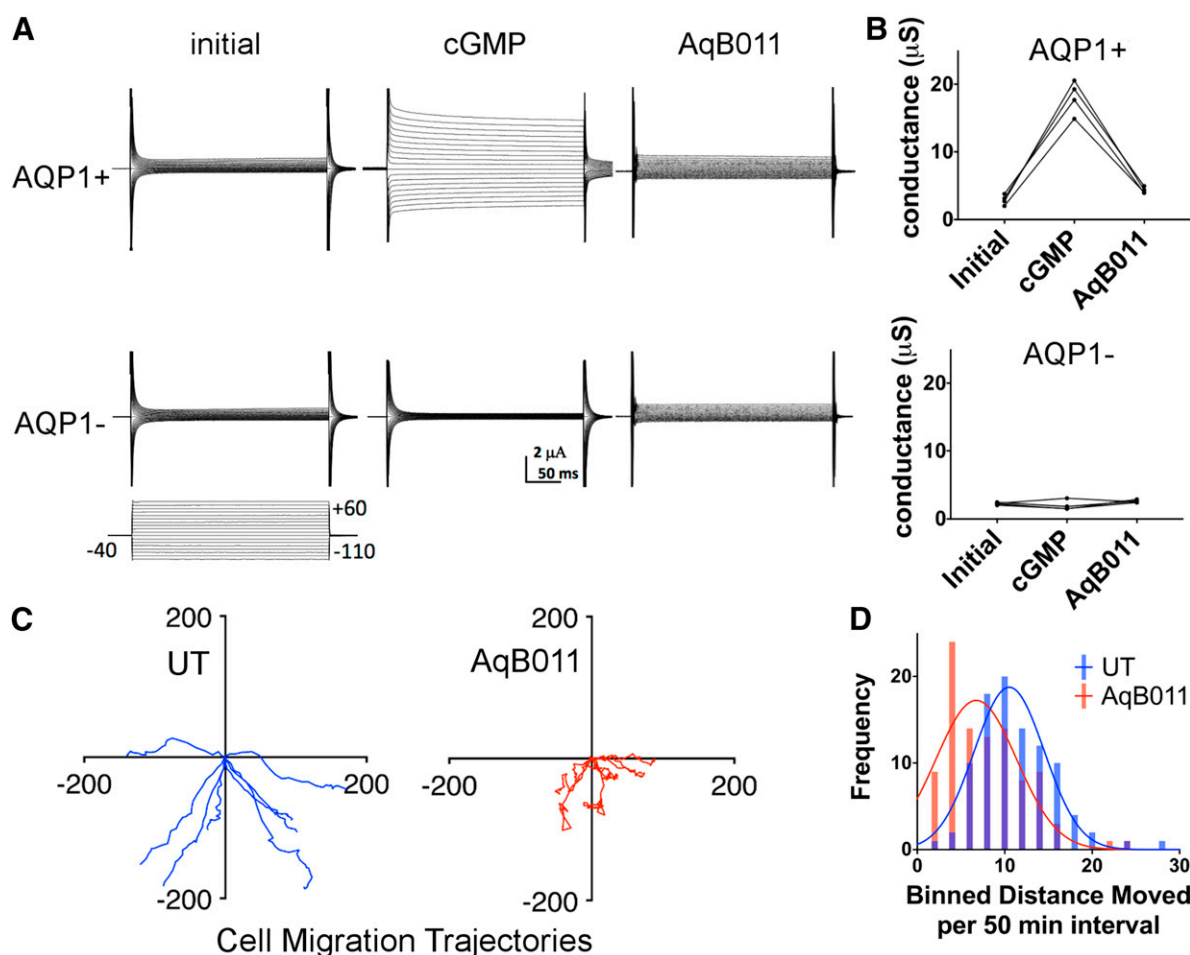


Fig. 2. AQP1 ion channels are permeable to Li^+ and blocked by the pharmacological agent AqB011, which also impairs migration in an AQP1-expressing cancer cell line. (A) Two-electrode voltage clamp recordings in Li^+ isotonic saline of human AQP1-expressing (AQP1+) and nonexpressing control (AQP1-) *Xenopus* oocytes. After initial recordings (initial), ionic conductance responses were activated in AQP1+ but not AQP1- oocytes by 25 minutes after application of CPT-cGMP (cGMP). Post incubation in AqB011 (30 μM ; 2 hours), the AQP1 conductance was unresponsive to the second application of cGMP (AqB011). (B) Trend plots illustrate responses for AQP+ oocytes measured before (initial) and after the first application of chlorophenylthio-cGMP (cGMP), and after the second application of CPT-cGMP following 2-hour incubation in saline with AqB011. Ion conductance responses were not observed in AQP1 control oocytes. (C) Migration trajectories for individual HT29 cells were monitored by live cell imaging at 50-minute intervals over 24 hours with (AqB011) and without AqB011 (UT) (80 μM). $n = 8$ cells per treatment. (D) Compiled Gaussian distributions of individual cell distances moved per 50-minute interval and illustration of impaired rates of migration in the AqB011-treated HT29 cells (mean \pm S.E.M. was $5.69 \pm 0.54 \mu\text{m}/\text{h}$ with AqB011 and $8.83 \pm 0.22 \mu\text{m}/\text{h}$ with AqB011; $n = 8$ per treatment group). UT, untreated.

cGMP (chlorophenylthio-cGMP; see *Materials and Methods* for details), demonstrating Li^+ permeability of the ion conductance in AQP1-expressing oocytes and not in control oocytes. Oocytes were then incubated 2 hours in 30 μM AqB011 and tested for reactivation by cGMP ("AqB011") in Li^+ saline. Results (Fig. 2B) showed that approximately 90% of the cGMP-induced current in AQP1-expressing oocytes was successfully blocked by AqB011, whereas control oocytes (AQP1⁻) lacked appreciable cGMP-activated current responses and showed no effect of the AqB011 inhibitor.

AqB011 Blocks Migration in AQP1-Expressing HT29 Colon Cancer Cells. Live-cell imaging was used to map the trajectories of cultured HT29 cells (Fig. 2C) to quantify migration rates in the presence and absence of the AQP1 ion channel blocker AqB011. Histogram summaries of the distances moved by individual cells per unit time interval show that the Gaussian distribution was substantially shifted to shorter distances in the presence of the AQP1 inhibitor (Fig. 2D), demonstrating that block of the ion channel activity impaired cell migration.

Li^+ Entry through Hot Spots in AQP1-Expressing HT29 Cells. The ability of SHL to detect Li^+ in live cells was

investigated using confocal microscopy. HT29 colon cancer cells are known to have high AQP1 expression (Pei et al., 2016b) and were chosen as a useful model for testing cellular imaging of Li^+ permeation through nonselective cation channels. SHL (50 μM in physiologic saline) was incubated with the HT29 cells for 2 hours prior to imaging to allow loading of SHL into the cells. The cells were counterstained with Hoechst 33258 to label nuclei.

Illumination with green laser light activated the MC(SHL)- Li^+ complex, which resulted in a red fluorescence signal characteristic of this chemical interaction (Fig. 3A, ON1). Exposure of the cells to continuous white light for 10 minutes progressively shifted the signal to a low level of fluorescence, consistent with the expected photoswitching from the fluorescent MC(SHL)- Li^+ complex to the nonfluorescent SP isomer. After prolonged white light illumination, the probe was reset to a responsive state by 10-minute recovery in darkness, which allowed reactivation of the probe signal (ON2). Fluorescence intensity decreased as a single-phase decay function over time when cells were illuminated with standard white light (Fig. 3B), as illustrated by images taken at 2-minute intervals. The normalized signal intensity decreased from 100 relative

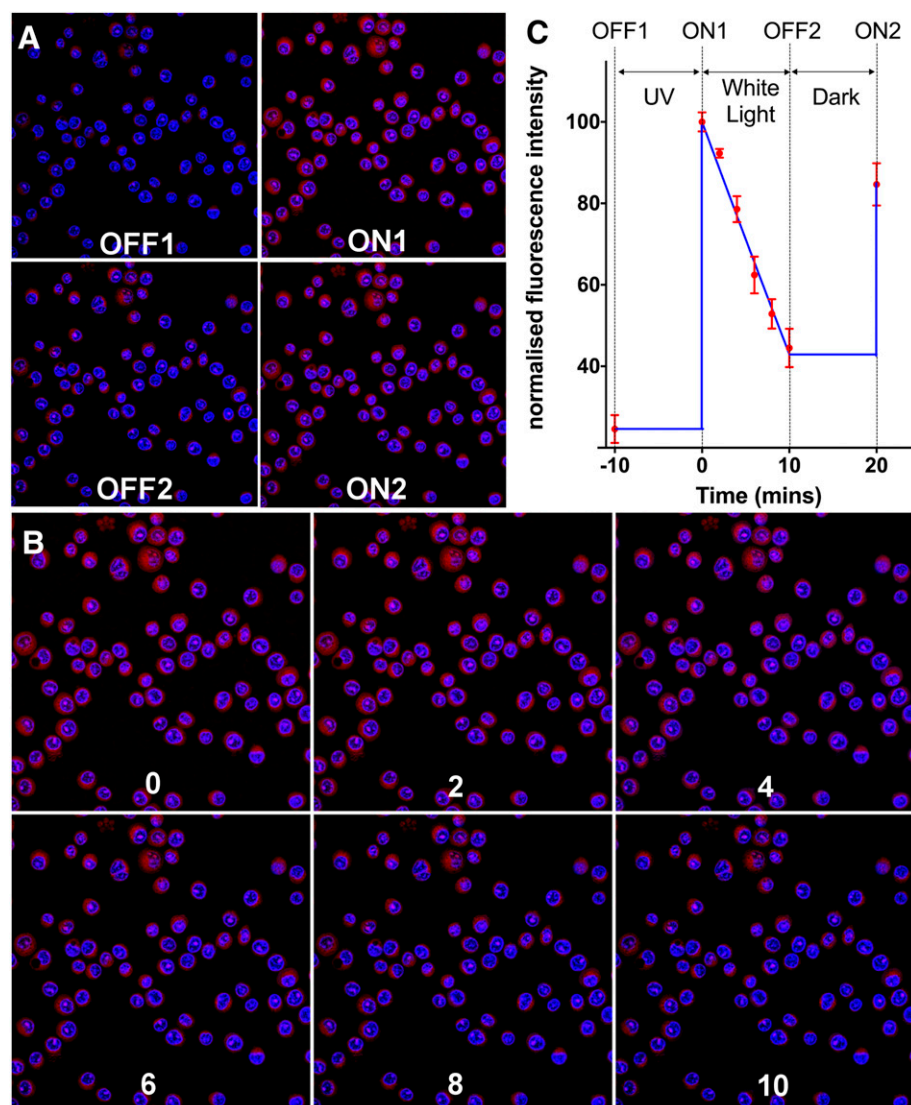


Fig. 3. Confocal time series for SHL signals in HT29 cells. (A) HT29 cells were incubated with 50 μM SHL for 2 hours prior to imaging. Cell nuclei were labeled with Hoechst 33258 (blue). Four distinctive states of the sensor during the photoswitch cycles are illustrated. Cells were first illuminated under visible light radiation for 10 minutes to convert the majority of the sensor back to nonfluorescent SP isomer (OFF1). Then, cells were illuminated under UV light for 10 minutes to convert SP isomer to fluorescent MC(SHL)- Li^+ complex (ON1), followed by exposure under white light for 10 minutes with measurement taken every 2 minutes (OFF2). Finally, cells were incubated in the dark for 10 minutes to allow the formation of the MC isomer and the binding of Li^+ to form the MC(SHL)- Li^+ complex (OFF2). (B) Ten-minute white light illumination was applied to cells after ON1 state; images were taken every 2 minutes as illustrated. Red SHL signals gradually faded with time. (C) Red fluorescent signals were measured for individual cells in the field of view, and values were normalized to ON1 state. Data are the mean \pm S.E.M.; the n value is 43. A single-phase decay function was fitted to values between ON1 (100%) and OFF2 (44.51%) states; the half-life was determined to be 4.13 minutes, with a τ value estimated at 5.95 minutes. After 10-minute incubation in the dark, sensors converted back to the MC isomer, and the normalized intensity increased from 44.51% (OFF2) to 84.65% (ON2).

fluorescence units (RFUs) to 44.51 RFUs after 10 minutes of visible light radiation (Fig. 3C). Under these experimental conditions, the half-life was determined to be 4.13 minutes with a τ value estimated at 5.95 minutes. Recovery in darkness for 10 minutes allowed the formation of the MC isomer. The binding of Li^+ regenerated the MC(SHL)- Li^+ complex at a normalized intensity of 84.65 RFUs (Fig. 3C; ON2). Repeated cycles of photoswitching performed on the same cells gave reproducible changes in fluorescence, demonstrating the ability of SHL to photoswitch reversibly in living cells. This innovation defines a new probe for monitoring changes in intracellular Li^+ in a biologic sample over time without loss of sensitivity imposed by photobleaching of a sensor. The photoswitching property allows repeated comparisons of function across multiple experimental treatments and provides additional advantages for biologic assays in which sample availability can be limited.

Distinctive punctate signals, referred to here as lithium “hot spots,” were observed in HT29 cells when imaged in Li^+ -containing saline (Fig. 4A, 1). A loss of hot spot events was observed after treatment with the AQP1 ion channel antagonist AqB011 (20 μM for 2 hours), after which only a faint background fluorescence was observed (Fig. 4A, 2). The removal of Li^+ from the extracellular saline by equimolar substitution with the TEA^+ ion also caused a loss of hot spots (Fig. 4A, 3), showing that the observed events resulted from Li^+ ion entry. In saline with TEA^+ , application of the blocker AqB011 had no additional effect on hot spot activity (Fig. 4A, 4). The fluorescent signal for the entire cell was reduced 2-fold in HT29 cells when Li^+ entry was compromised by pharmacological block of the ion channel with AqB011 or by removal of extracellular Li^+ ion via replacement with other cations as chloride salts (Fig. 4B). Collectively, these data confirmed that the bright punctate Li^+ signals depended on the presence of extracellular Li^+ and the presence of functional AQP1 ion channels, and ruled out the possibility that hot spots were indirectly due to nonspecific interactions with other intracellular cations or entry of Li^+ through other cation pathways. The most parsimonious interpretation is that the lithium hot spots represent Li^+ entry across the plasma membrane through AQP1 cation channels.

Knockdown of AQP1 expression with small interfering RNA (siRNA) resulted in a dramatic loss of red Li^+ hot spots, specifically in transfected HT29 cells (labeled green with cotransfected siGLO transfection indicator) and not in nontransfected cells in the same culture plate (Fig. 4C). The fluorescence intensity of signals from the SHL Li^+ probe (Fig. 4D) and the levels of AQP1 transcript assessed by quantitative PCR (Fig. 4E) both were reduced significantly with AQP1-siRNA treatment, but not with control scrambled siRNA treatment. These data confirm that in HT29 cells, the appearance of Li^+ hot spots requires the expression of AQP1 channels.

Li^+ Hot Spots Were Not Observed in SW620 Cells Lacking High Levels of AQP1 Expression. The role of AQP1 ion channels in mediating the lithium hot spot events was tested by comparison with another colon cancer cell line (SW620) which is similar to HT29 in having an adherent epithelial phenotype (Fogh et al., 1977) but different in that rates of migration are slower. Levels of AQP1 expression were approximately 2.6-fold lower in SW620 than in HT29 cells (Fig. 5, A and B); this finding is further supported by the reverse-transcription PCR data (Fig. 5C). HT29 cells and

SW620 cells were preincubated in SHL for 2 hours, transferred into Li^+ -substituted saline, and imaged. Results show that the lithium hot spots are more abundant and brighter in HT29 cells (Fig. 5D, 1–3) than in SW620 cells (Fig. 5D, 4–6). In migrating HT29 cells, lithium hot spots are concentrated in leading edges (Fig. 5D, 2 and 3) in contrast to the uniform distribution seen in nonmigrating cells (Fig. 5D, 1). This observation is consistent with the known clustering of AQP1 channels in the leading edges of specific classes of cells during migration (McCoy and Sontheimer, 2007), where these channels are proposed to facilitate fluid movements needed for volume changes during extension, and possibly to compensate for changes in osmotic pressure associated with actin polymerization and depolymerization (Hu and Verkman, 2006).

AQP1 expression and localization were determined by immunofluorescent imaging using confocal microscopy. AQP1 protein was immunolabeled with anti-AQP1 primary antibody and green fluorescent AlexaFluor 488 secondary antibody and visualized by 488-nm laser excitation. HT29 cells demonstrated high AQP1 signal intensities as compared with SW620 cells (Fig. 6, A and B). Comparison with SW620 cells confirmed that a reduced abundance of lithium hot spots correlated with lower levels of AQP1 expression. In combination, results here based on pharmacology, ion substitution, and a comparison of cell lines with different levels of AQP1 expression provide evidence that the lithium hot spots measured by the novel probe SHL mark the locations of active AQP1 ion channels.

Lithium Hot Spots Are Colocalized with AQP1 Channels in HT29 Cells. The spatial correlation between the locations of the lithium hot spots and AQP1 channels was assessed using confocal microscopy. Signal intensities using Z-stack compiled images were measured as a function of distance across the cell diameter (indicated by straight lines crossing the cell centers; two cross-sections per cell). Signals were plotted as a function of X-Y distance to quantify the correspondence between the SHL Li^+ fluorescence intensity [red channel; MC(SHL)- Li^+ complex] and the AQP1 protein signal intensity (green channel; immunofluorescence). Results in Fig. 6C show that the two fluorescence signals were strongly colocalized in HT29 cells (with superimposed red and green signals represented as yellow), yielding RFUs ranging from 50 to 200 that were consistent with data shown in Fig. 5A. The spatial profiles of the red and green signals across the cell diameter are illustrated by plots of signal intensity (Fig. 6D). Li^+ and AQP1 signals in HT29 cells were strongly correlated, with R^2 values ranging 0.61 to 0.68. In contrast, SW620 cells (Fig. 6D) showed low signal intensities and poor spatial correlation, with signal values mainly at 0–50 RFUs and R^2 values ranging from 0.06 to 0.09. This work opens new avenues for the potential real-time visualization of cation channel function and the localization of active channel domains in living cells, and provides additional insight into the relevance of cation channels such as AQP1 in dynamic cellular responses, such as migration.

Lithium Hot Spots Are Dynamic When Imaged in HT29 Cells. The ability of SHL to detect dynamic Li^+ entry through AQP1 was tested using a 300-second time-lapse video of an SHL-loaded cell directly after perfusion with Li^+ -substituted extracellular saline. The intensity of Li^+ hot spots increased during the first half of the recording, then cycled between increasing and decreasing signal intensities during the second half (Fig. 7). The montage shows a time series for a $2 \times 3\text{-}\mu\text{m}$ field of view (rectangle), illustrating the dynamic fluorescence

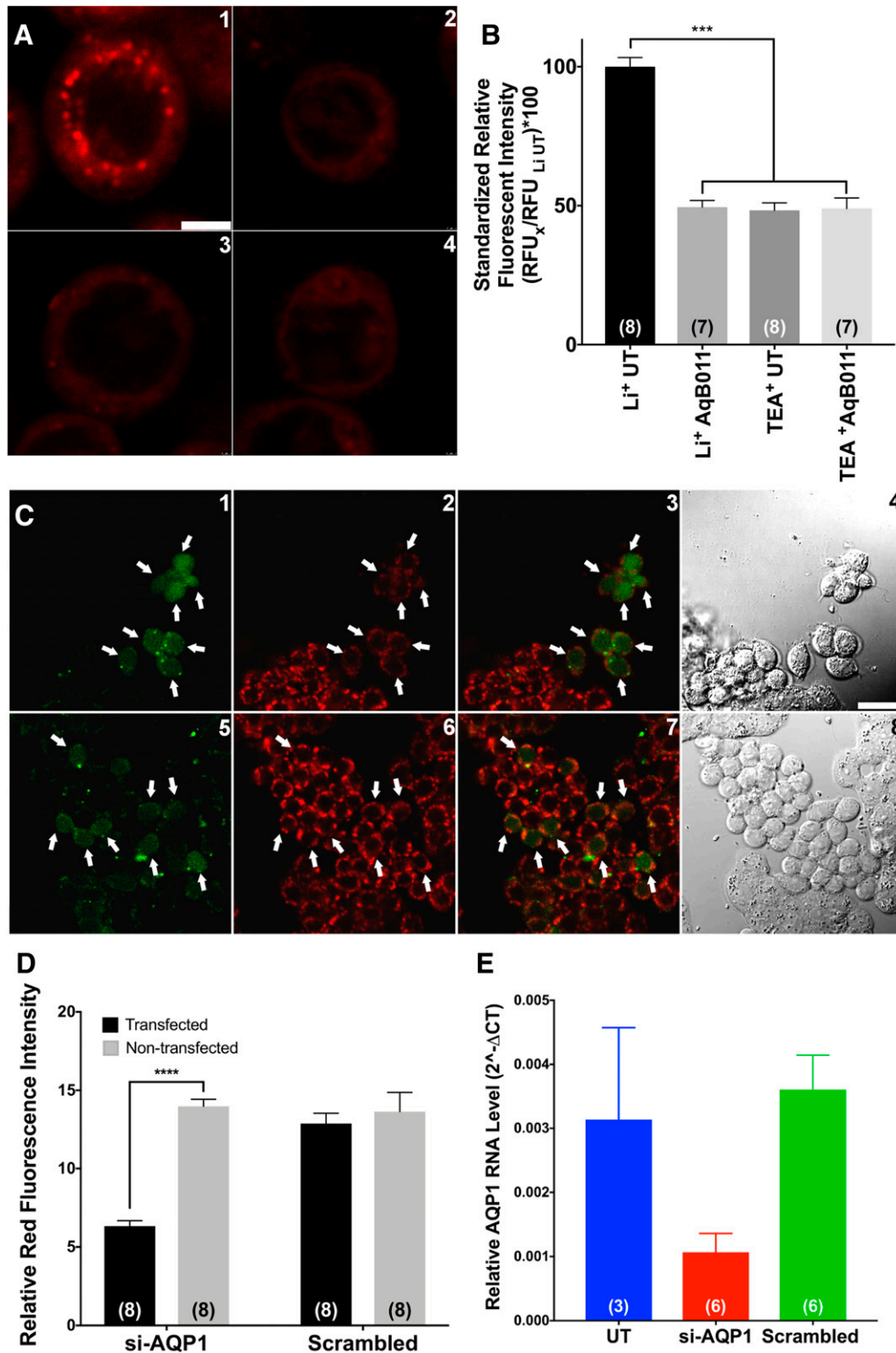


Fig. 4. Lithium hot spot signals depend on functional AQP1 channels. (A) Distinctive punctate Li^+ hot spots were observed in HT29 cells imaged in Li^+ -substituted extracellular saline (1). In cells that were pretreated with $20 \mu\text{M}$ AqB011 for 2 hours, Li^+ hot spots were not observed (2). Similar losses of hot spot events were observed after the removal of Li^+ from the extracellular saline by equimolar substitution of TEA^+ (3). Pretreatment with $20 \mu\text{M}$ AqB011 (2 hours) caused no further change in the signal in the absence of extracellular Li^+ (4). (B) Li^+ -selective fluorescent signals were quantified by measuring red fluorescence intensities of individual cells. Intensities were normalized to those of HT29 cells imaged in Li^+ saline. Li^+ entry was significantly compromised by pharmacological block (AqB011) or removal of Li^+ ion from the saline by equimolar replacement with other cations, such as TEA^+ . Significant differences were analyzed by comparing the Li^+ AqB011, TEA^+ UT, and TEA^+ AqB011 groups to the Li^+ UT group (see *Materials and Methods* for details). (C) HT29 cells were transfected with either siRNA targeting AQP1 (si-AQP1, upper panels) or scrambled siRNA (scrambled, lower panels) before confocal imaging. Cells were preincubated in transfection indicator siGLO Green (green, 1 and 5) and SHL (red, 2 and 6). Stacked images of both green and red channels are illustrated in 3 and 7, and bright field images are illustrated in 4 and 8. Li^+ signals were impaired in cells successfully transfected with AQP1 siRNA (cells with green nucleus, 3) but not in cells transfected with scrambled siRNA (cells with green nucleus, 7). (D) Li^+ -selective

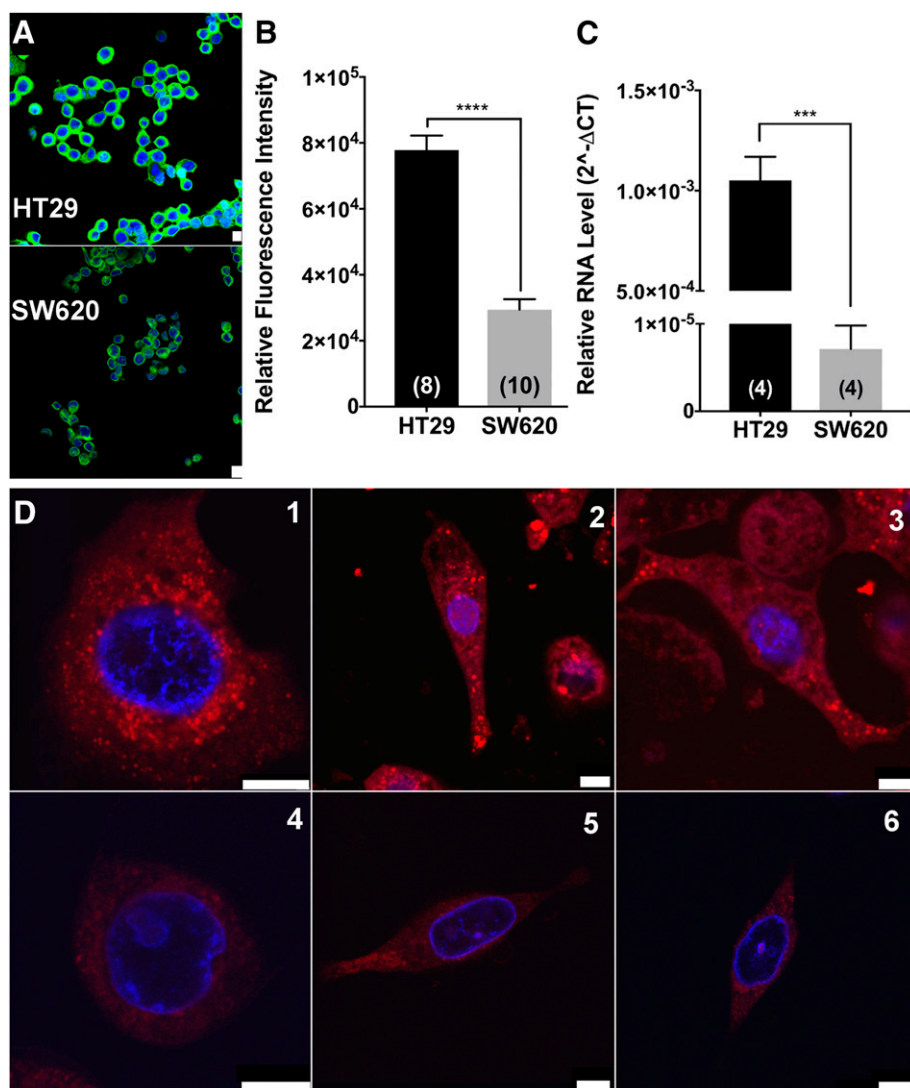


Fig. 5. Characterization of lithium hot spots in AQP1-expressing and AQP1-deficient cells. (A) Cells were labeled with Hoechst nuclear stain (blue) and anti-AQP1 antibody (tagged with fluorescent secondary antibody; green). (B) Anti-AQP1 immunofluorescence intensities for HT29 cells were approximately 2.6-fold higher than in SW620 cells. (C) AQP1 RNA levels measured by reverse-transcription quantitative PCR were more than 100-fold lower in SW620 cells as compared with HT29 cells. (D) HT29 and SW620 cells were loaded with SHL for 2 hours prior to imaging. A strong Li⁺ signal was observed in all HT29 cells (1, 2, 3) as compared with the minimal Li⁺ signals observed in SW620 cells (4, 5, 6). In nonmigrating HT29 cells, Li⁺ hot spots appeared as widely distributed across the cell (1). In migrating HT29 cells, Li⁺ hot spots were concentrated at leading edges of the cells (2, 3). White scale bars indicate 5 μ m. Significant differences were analyzed by unpaired *t* test and are reported as $P < 0.001$ (***) (see *Materials and Methods* for details).

emission properties. A movie depicting Li⁺ hot spot activity in HT29 cells in real time is available as Supplemental Material (Supplemental Video).

Discussion

Work with confocal imaging presented here is the first to demonstrate the use of a new Li⁺-selective photoswitchable probe as a tool for monitoring nonselective cation entry in living cells, with AQP1 ion channels of migrating cancer cells selected as a model for illustrating feasibility and potential significance. Nonselective monovalent cation channel activity was monitored with the probe SHL, which is selective for Li⁺. Lithium hot spots were abundant in HT29 colon cancer cells expressing high levels of AQP1 and rare in SW620 colon cancer cells which have comparatively little AQP1. The spatial

localization of Li⁺ hot spots at the leading edges of HT29 cells was an exciting observation, fitting the predicted location of AQP1 ion channels. Future studies characterizing the dynamic temporal and spatial properties of ion fluxes in migrating cells at higher resolution will be of interest.

The initial proposal that AQP1 works as a nonselective cation channel in addition to its known role as a water channel (Yool et al., 1996) generated controversy (Agre et al., 1997; Tsunoda et al., 2004). Subsequent analyses confirmed the capacity of AQP1 to function as a dual water and ion channel, showing the ion channel activity was gated directed by intracellular cGMP and indirectly regulated by intracellular signaling cascades including tyrosine phosphorylation (Anthony et al., 2000; Saparov et al., 2001; Boassa and Yool, 2003; Campbell et al., 2012), but left unclear the physiologic relevance of the dual water and ion channel function (Saparov et al., 2001). Recent work has since

fluorescent signals were quantified by measuring red fluorescent intensities of individual cells that were either transfected (green nucleus signal) or nontransfected (no nucleus signal). Li⁺ entry was significantly impaired in cells with AQP1 knockdown. Significant differences were analyzed by one-way ANOVA with post hoc Bonferroni tests and are reported as $P < 0.0001$ (****). (E) AQP1 RNA levels were quantified by using reverse-transcription PCR. AQP1 RNA levels were lowered in cells transfected with siRNA targeting AQP1 compared with either cells without transfection (UT) or cells with scrambled siRNA transfection (scrambled). UT, untreated.

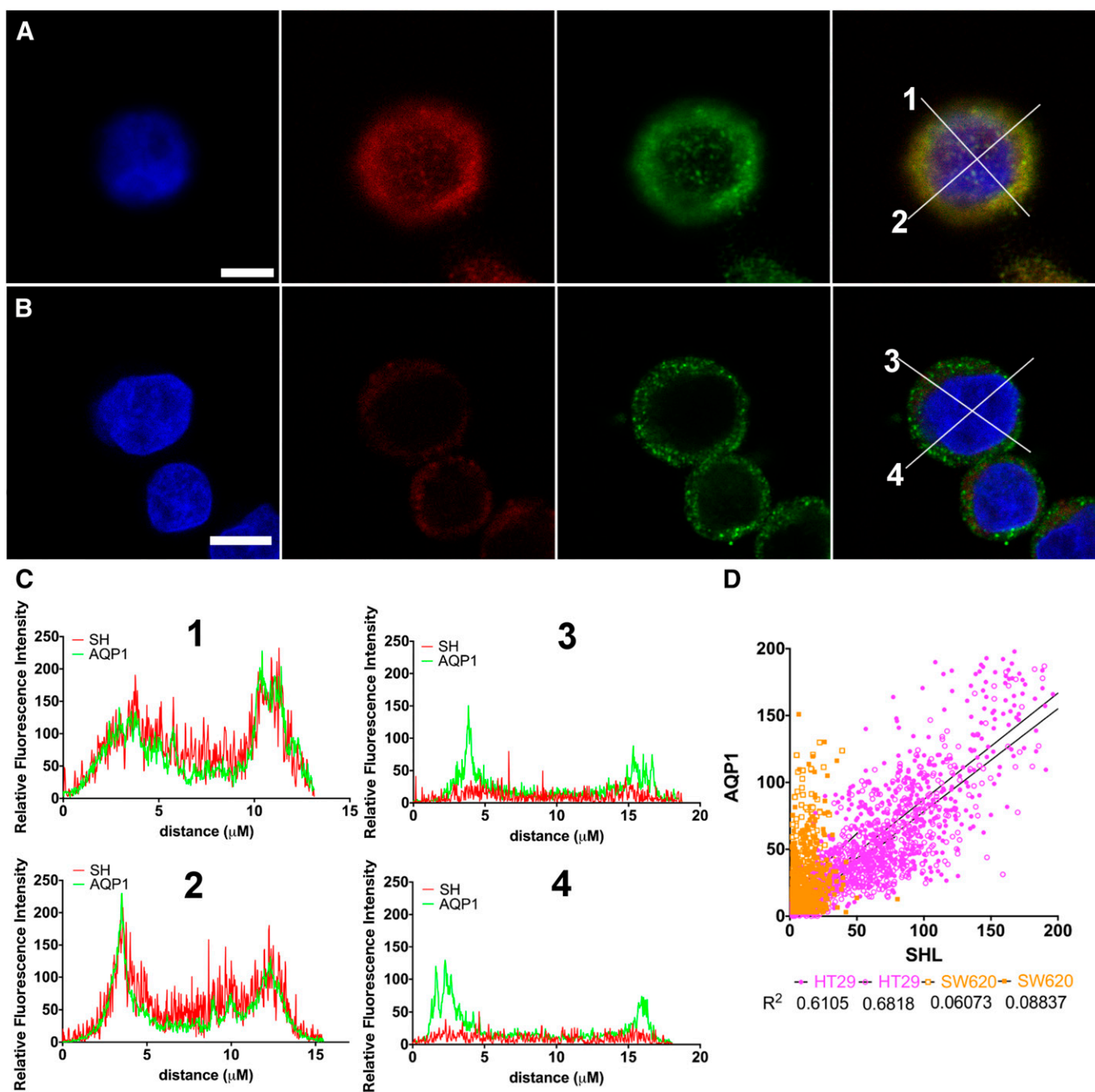


Fig. 6. Quantitative confocal analyses of the colocalization of AQP1 and Li^+ hot spots. HT29 cells (A) and SW620 cells (B) were preincubated with SHL (red) and then fixed and labeled with AQP1 primary antibody and AlexaFluor-488-conjugated secondary antibody (green). Nuclei were stained with Hoechst (blue). Both the Li^+ and AQP1 signals were at higher intensities in HT29 cells than in SW620 cells. In the far-right panels, all three signal bandwidth images are combined, with colocalized red and green signals seen as yellow. Fluorescence signals from the MC(SHL)- Li^+ complex and AQP1 were strongly colocalized in HT29 cells but not in SW620 cells. (C) Two cross-sections through cell centers were selected (labeled 1 and 2 for HT29, 3 and 4 for SW620). The red Li^+ and green AQP1 signal intensities in the cross-sectional lines were plotted as a function of X-Y distance across the cell. HT29 cells showed robust levels and a strong correlation between Li^+ and AQP1 signal intensities, which was not seen in SW620 cells. (D) Linear regression analyses quantified the correlation between Li^+ signal and AQP1 signal intensities in HT29 cells (pink) and SW620 cells (orange) for data from (C). R^2 values calculated using GraphPad Prism 7 were 0.61 and 0.68 for HT29 cell cross sections, and 0.06 and 0.09 for SW620 cells.

demonstrated that the AQP1 ion conductance is essential for rapid cell movement in a subset of cancer cells which show high metastasis or invasiveness (Kourghi et al., 2016; Pei et al., 2016b), demonstrating a functional role for the AQP1 ion channel.

AQP1 channels are not the only pathway for Li^+ transport across cell membranes. Li^+ is also conducted through

voltage-gated Na^+ channels (Hille, 1972; Richelson, 1977; Timmer and Sands, 1999) and the Na^+ -proton exchanger (Lenox et al., 1998). Some of the Li^+ signal described here could involve additional channels or transporters. However, the alternative hypothesis that the lithium signal observed in HT29 cancer cells is due entirely to mechanisms unrelated to

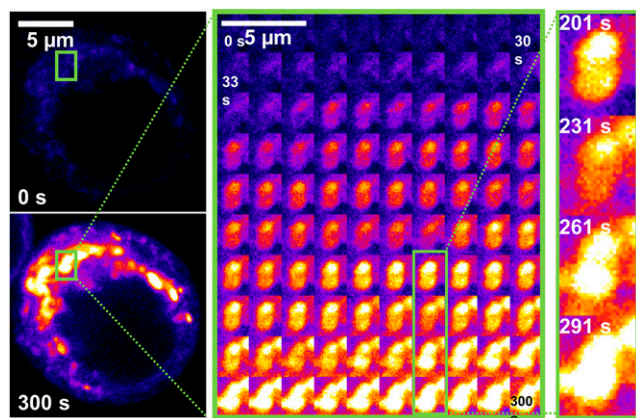


Fig. 7. Dynamic properties of Li^+ hot spots illustrating ON/OFF SHL probe transitions in a living HT29 cell. HT29 cells preloaded with SHL were imaged for 100 frames at 3-second intervals. Extracellular saline was replaced with Li^+ saline at time 0. Multiple Li^+ hot spots were activated, as illustrated in the left panels at time 0 and 300 seconds. Images were cropped to show higher magnification views of two discrete Li^+ hot spots (middle panel) as a time-lapse montage, illustrating the independent ON/OFF/ON transitions of the hot spots (inset, right).

AQP1 seems unlikely for several reasons. First, results here show that pharmacological inhibition with the AQP1 ion channel blocker AqB011 significantly diminished the Li^+ signal to a level similar to the response observed in cells imaged in saline with TEA^+ (which does not bind to SHL). Other AQP modulators in the library of bumetanide derivatives that include AqB011 have been shown to be selective for specific AQP classes without off-target effects on other signaling and transport mechanisms (Migliati et al., 2009; Yool et al., 2013). Second, the punctate Li^+ signal pattern was not evident in SW620 cells that have low levels of AQP1 expression but otherwise express various channels and transporters required for basic cellular function and low-level motility. Third, the colocalization of AQP1 expression and Li^+ signals showed a robust correlation.

Since SHL passively diffuses across the membrane, it should achieve a reasonably uniform distribution on the cytoplasmic side. Punctate Li^+ hot spots indicate local areas of Li^+ entry and accumulation. As shown using the oocyte expression system, AQP1 ion channels mediate Li^+ influx. In combination with results of pharmacological block and siRNA knockdown, data here support the interpretation that the interaction of Li^+ with SHL resulting in hot spots occurs in the vicinity of active AQP1 ion channels. The remaining intracellular SHL throughout areas without substantial Li^+ influx would remain predominantly in the nonfluorescent form, consistent with the low-level background fluorescence.

The increased incidence of hot spots in cellular protrusions was consistent with work from others indicating that AQP1 is localized at the leading edges in migrating cells (McCoy and Sontheimer, 2007). The slow temporal resolution used here for image capture was sufficient to illustrate the dynamic property of the Li^+ hot spots, which turned on and off over time (as shown in Fig. 7). The observed on/off dynamics of SHL in AQP1-expressing cells was limited by our confocal microscopy setup to a minimal image acquisition rate of 3 seconds per frame; optimization will be needed to enable better evaluations of channel kinetics. Our focus on AQP1 for testing the SHL probe may have benefitted from the usually slow gating properties of the AQP1 ion channel, which once

opened, shows long bursts persisting for hundreds of milliseconds and sets of bursts lasting for seconds (Anthony et al., 2000).

Evidence that AQP1 is not just a water channel but also functions as a monovalent cation channel contributes to our understanding of the diverse mechanisms that govern cell migration. Looking ahead to translational applications, we propose that the lithium sensor will be useful for investigating cation channel function in many types of living cells, including sensory cells, immune cells, cancer cells, and more. The AQP1 ion channel itself is an attractive candidate for development of new therapeutics, and the Li^+ sensor SHL could be a powerful tool in high-throughput screening for new pharmacological agents that might ultimately help manage metastasis in aggressive AQP1-dependent cancers.

Acknowledgments

The authors acknowledge Dr. Xiaozhou Zhang for useful discussions, and Dr. Agatha Labrinidis and Dr. Jane Sibbons at Adelaide Microscopy for training and access to core microscopy facilities.

Authorship Contributions

Participated in research design: Pei, Heng, Abell, Yool.
Conducted experiments: Pei, Heng, De Ieso, Sylvia, Kourghi, Nourmohammadi.
Contributed new reagents or analytic tools: Pei, Heng, Abell.
Performed data analysis: Pei, Heng, De Ieso, Sylvia, Kourghi, Nourmohammadi, Yool.
Wrote or contributed to the writing of the manuscript: Pei, Heng, De Ieso, Sylvia, Kourghi, Nourmohammadi, Abell, Yool.

References

- Agre P, Lee MD, Devidas S, and Guggino WB (1997) Aquaporins and ion conductance. *Science* **275**:1490, author reply 1492.
- Agre P, Preston GM, Smith BL, Jung JS, Raina S, Moon C, Guggino WB, and Nielsen S (1993) Aquaporin CHIP: the archetypal molecular water channel. *Am J Physiol* **265**:F463–F476.
- Anthony TL, Brooks HL, Boassa D, Leonov S, Yanocho GM, Regan JW, and Yool AJ (2000) Cloned human aquaporin-1 is a cyclic GMP-gated ion channel. *Mol Pharmacol* **57**:576–588.
- Boassa D and Yool AJ (2003) Single amino acids in the carboxyl terminal domain of aquaporin-1 contribute to cGMP-dependent ion channel activation. *BMC Physiol* **3**:12.
- Campbell EM, Birdsell DN, and Yool AJ (2012) The activity of human aquaporin 1 as a cGMP-gated cation channel is regulated by tyrosine phosphorylation in the carboxyl-terminal domain. *Mol Pharmacol* **81**:97–105.
- Dorward HS, Du A, Bruhn MA, Wrin J, Pei JV, Evdokiou A, Price TJ, Yool AJ, and Hardingham JE (2016) Pharmacological blockade of aquaporin-1 water channel by AqB013 restricts migration and invasiveness of colon cancer cells and prevents endothelial tube formation in vitro. *J Exp Clin Cancer Res* **35**:36.
- Fogh J, Fogh JM, and Orfeo T (1977) One hundred and twenty-seven cultured human tumor cell lines producing tumors in nude mice. *J Natl Cancer Inst* **59**:221–226.
- Friedl P and Wolf K (2003) Tumour-cell invasion and migration: diversity and escape mechanisms. *Nat Rev Cancer* **3**:362–374.
- Heng S, Mak AM, Kostecky R, Zhang X, Pei J, Stubing DB, Ebendorff-Heidepriem H, and Abell AD (2017) Photoswitchable calcium sensor: ‘On’-‘Off’ sensing in cells or with microstructured optical fibers. *Sens Actuators B Chem* **252**:965–972.
- Heng S, Nguyen M, Kostecky R, Monro TM, and Abell AD (2013) Nanoliter-scale, regenerable ion sensor: sensing with a surface functionalized microstructured optical fiber. *RSC Adv* **3**:8308–8317.
- Hille B (1972) The permeability of the sodium channel to metal cations in myelinated nerve. *J Gen Physiol* **59**:637–658.
- Hu J and Verkman AS (2006) Increased migration and metastatic potential of tumor cells expressing aquaporin water channels. *FASEB J* **20**:1892–1894.
- King LS, Kozono D, and Agre P (2004) From structure to disease: the evolving tale of aquaporin biology. *Nat Rev Mol Cell Biol* **5**:687–698.
- Klajn R (2014) Spiropyran-based dynamic materials. *Chem Soc Rev* **43**:148–184.
- Kolmakov K, Belov VN, Bierwagen J, Ringemann C, Müller V, Eggeling C, and Hell SW (2010) Red-emitting rhodamine dyes for fluorescence microscopy and nanoscopy. *Chemistry* **16**:158–166.
- Kourghi M, Pei JV, De Ieso ML, Flynn G, and Yool AJ (2016) Bumetanide derivatives AqB007 and AqB011 selectively block the aquaporin-1 ion channel conductance and slow cancer cell migration. *Mol Pharmacol* **89**:133–140.
- Krummel MF, Bartumeus F, and Gérard A (2016) T cell migration, search strategies and mechanisms. *Nat Rev Immunol* **16**:193–201.
- Lenox RH, McNamara RK, Papke RL, and Manji HK (1998) Neurobiology of lithium: an update. *J Clin Psychiatry* **59** (Suppl 6):37–47.
- McCoy E and Sontheimer H (2007) Expression and function of water channels (aquaporins) in migrating malignant astrocytes. *Glia* **55**:1034–1043.

- Migliati E, Meurice N, DuBois P, Fang JS, Somasekharan S, Beckett E, Flynn G, and Yool AJ (2009) Inhibition of aquaporin-1 and aquaporin-4 water permeability by a derivative of the loop diuretic bumetanide acting at an internal pore-occluding binding site. *Mol Pharmacol* **76**:105–112.
- Olson MF and Sahai E (2009) The actin cytoskeleton in cancer cell motility. *Clin Exp Metastasis* **26**:273–287.
- Papadopoulos MC, Saadoun S, and Verkman AS (2008) Aquaporins and cell migration. *Pflugers Arch* **456**:693–700.
- Pei JV, Burton JL, Kourghi M, De Ieso ML, and Yool AJ (2016a) Drug discovery and therapeutic targets for pharmacological modulators of aquaporin channels, in *Aquaporins in Health and Disease: New Molecular Targets for Drug Discovery* (Soveral G, Casinin A, and Nielsen S eds) pp 275–297, CRC Press, Oxfordshire, UK.
- Pei JV, Kourghi M, De Ieso ML, Campbell EM, Dorward HS, Hardingham JE, and Yool AJ (2016b) Differential inhibition of water and ion channel activities of mammalian aquaporin-1 by two structurally related bacopaside compounds derived from the medicinal plant bacopa monnieri. *Mol Pharmacol* **90**:496–507.
- Petrie RJ, Doyle AD, and Yamada KM (2009) Random versus directionally persistent cell migration. *Nat Rev Mol Cell Biol* **10**:538–549.
- Richelson E (1977) Lithium ion entry through the sodium channel of cultured mouse neuroblastoma cells: a biochemical study. *Science* **196**:1001–1002.
- Rivera-Fuentes P, Wrobel AT, Zastrow ML, Khan M, Georgiou J, Luyben TT, Roder JC, Okamoto K, and Lippard SJ (2015) A far-red emitting probe for unambiguous detection of mobile zinc in acidic vesicles and deep tissue. *Chem Sci (Camb)* **6**:1944–1948.
- Saparov SM, Kozono D, Rothe U, Agre P, and Pohl P (2001) Water and ion permeation of aquaporin-1 in planar lipid bilayers. Major differences in structural determinants and stoichiometry. *J Biol Chem* **276**:31515–31520.
- Smith E, Palethorpe HM, Tomita Y, Pei JV, Townsend AR, Price TJ, Young JP, Yool AJ, and Hardingham JE (2018) The purified extract from the medicinal plant *Bacopa monnieri*, bacopaside II, inhibits growth of colon cancer cells in vitro by inducing cell cycle arrest and apoptosis. *Cells* **7**.
- Stubing DB, Heng S, and Abell AD (2016) Crowned spiropyran fluoroionophores with a carboxyl moiety for the selective detection of lithium ions. *Org Biomol Chem* **14**:3752–3757.
- Timmer RT and Sands JM (1999) Lithium intoxication. *J Am Soc Nephrol* **10**:666–674.
- Tsunoda SP, Wiesner B, Lorenz D, Rosenthal W, and Pohl P (2004) Aquaporin-1, nothing but a water channel. *J Biol Chem* **279**:11364–11367.
- Yool AJ, Morelle J, Cnops Y, Verbavatz JM, Campbell EM, Beckett EA, Booker GW, Flynn G, and Devuyt O (2013) AqF026 is a pharmacologic agonist of the water channel aquaporin-1. *J Am Soc Nephrol* **24**:1045–1052.
- Yool AJ, Stamer WD, and Regan JW (1996) Forskolin stimulation of water and cation permeability in aquaporin 1 water channels. *Science* **273**:1216–1218.

Address correspondence to: Andrea J. Yool, Adelaide Medical School, Helen Mayo South, Frome Road, University of Adelaide, Adelaide 5005 Australia.
E-mail: andrea.yool@adelaide.edu.au

Molecular Pharmacology

Supplemental Data

for

Lithium ‘Hot-spots’: Real-time Analysis of non-selective cation channel activity in migrating cancer cells

Jinxin V Pei¹, Sabrina Heng², Michael De Ieso¹, Georgina Sylvia², Mohamad Kourghi¹, Saeed Nourmohammadi¹, Andrew D Abell², and Andrea J Yool¹

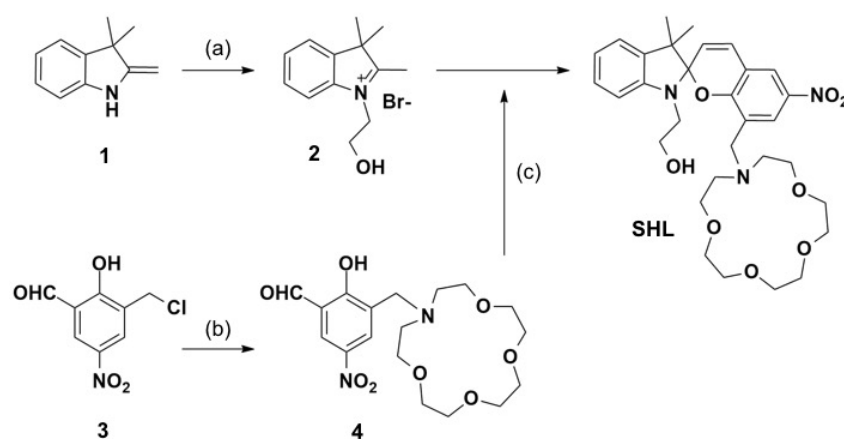
¹Adelaide Medical School, and the Institute for Photonics and Advanced Sensing (IPAS), The University of Adelaide, Adelaide, SA 5005, Australia.

²ARC Centre of Excellence for Nanoscale BioPhotonics (CNBP), IPAS, School of Physical Sciences, The University of Adelaide, Adelaide, SA 5005, Australia.

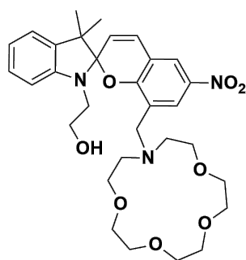
Supplemental Methods

General Methods and Materials for SHL Synthesis

All ^{13}C NMR spectra (126 MHz) and ^1H NMR spectra (500 MHz) were recorded on an Agilent Technologies 500 MHz NMR spectrometer with DD2 console in DMSO-d_6 . Chemical shifts (δ) are reported in ppm. Chemical shifts of DMSO-d_6 ($\delta_{\text{C}} = 39.52$ ppm) or TMS ($\delta_{\text{H}} = 0.0$ ppm) were used as internal standards in all ^{13}C NMR and ^1H NMR experiments, respectively. High resolution mass spectrometry was performed on the Agilent 6230 TOF LC-MS. HPLC grade acetonitrile was used in all related experiments. Compound **2**¹ and compound **4**² were prepared as previously described. All metal ions used in this work were in the form of perchlorate salt. All other reagents were purchased from Sigma-Aldrich and used without further purification.

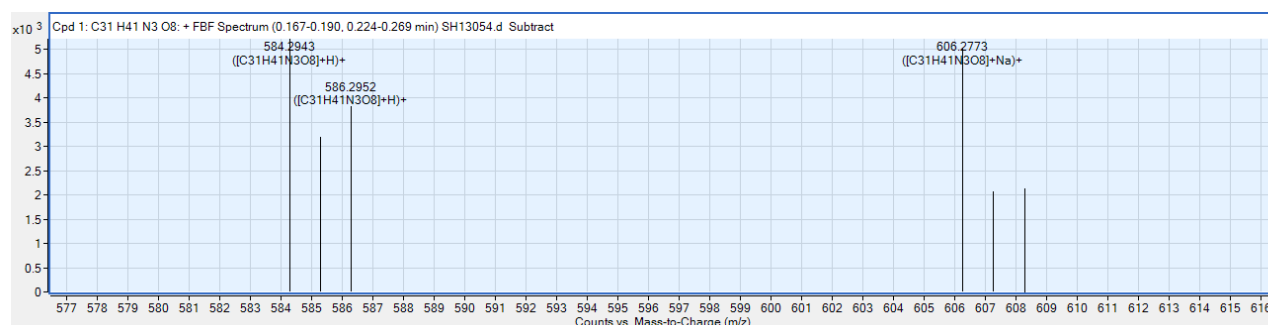


Supplemental Scheme 1. Synthesis of **SHL**. (a) 2-Bromoethanol, acetonitrile, reflux, 18 h; (b) 1-aza-15-crown-5, Et_3N , THF, $0\text{ }^\circ\text{C}$; (c) ethanol, reflux, 18 h.

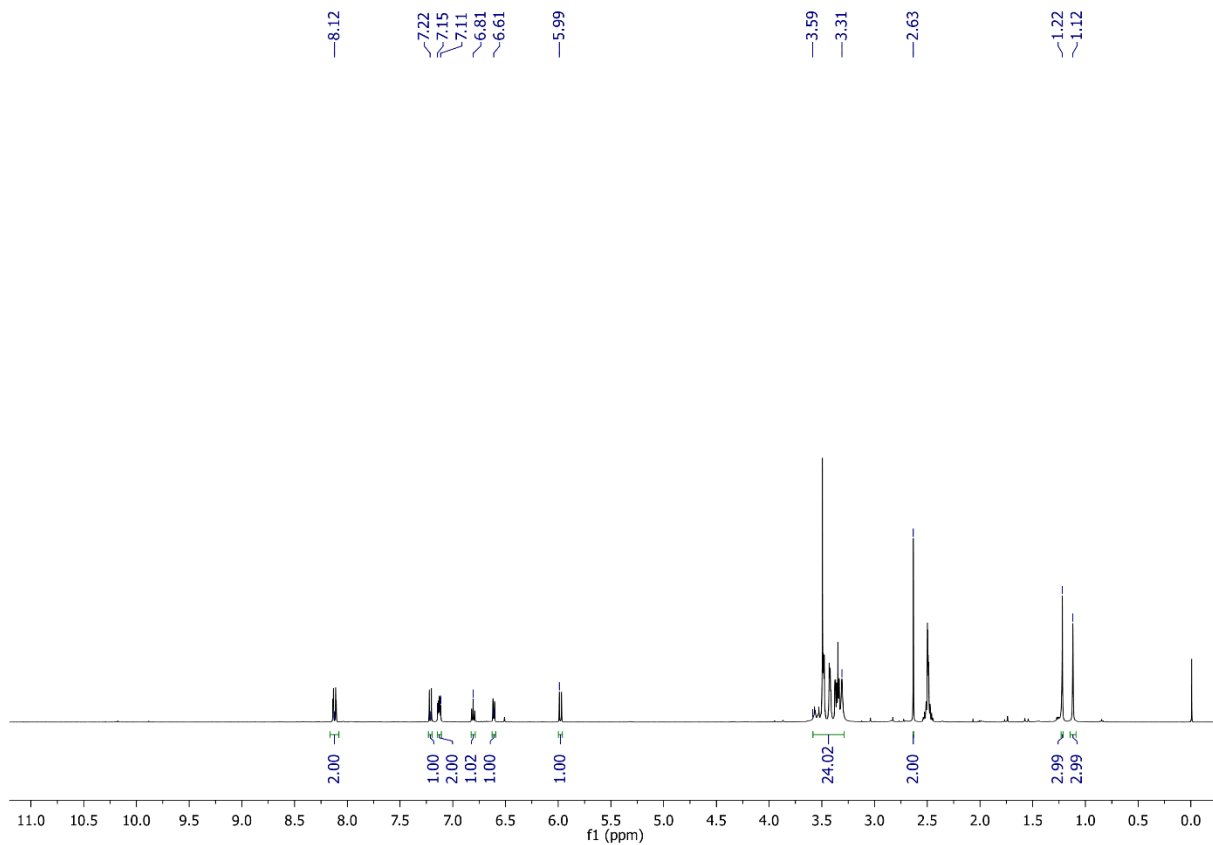


2-(8-((1,4,7,10-tetraoxa-13-azacyclopentadecan-13-yl)methyl)-3',3'-dimethyl-6-nitrospiro[chromene-2,2'-indolin]-1'-yl)ethanol (SHL).

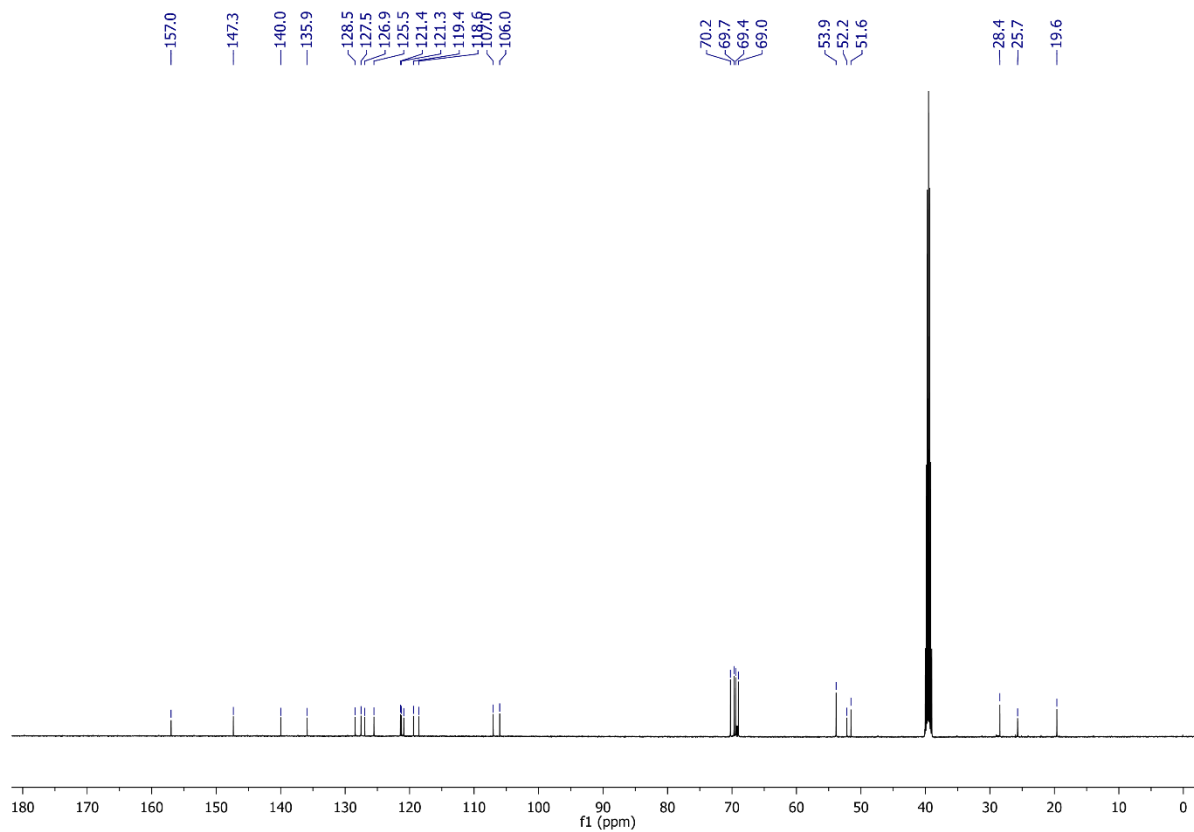
Compound **4**² (566 mg, 1.4 mmol) and indoline **2**¹ (230 mg, 1.1 mmol) were combined and dissolved in ethanol (10 mL) and the mixture was heated to reflux for 18 h. Excess solvent was removed *in vacuo* to give a purple crude solid (0.68 g) which was purified by C18 reverse phase silica chromatography eluting with 0 - 30% water / acetonitrile to give **SHL** as a purple solid (120 mg, 18 % yield). ¹H NMR (500 MHz, DMSO-d₆) δ 8.12 (dd, 2H, ArH, *J* = 12.5, 2.5 Hz), 7.22 (d, 1H, ArH, *J* = 10.5 Hz), 7.15 – 7.12 (m, 2H, ArH), 6.81 (t, 1H, ArH, *J* = 7.5 Hz), 6.61 (d, 1H, ArH, *J* = 7.5 Hz), 5.99 (d, 1H, ArH, *J* = 10.5 Hz), 3.59 – 3.31 (m, 24H, CH₂), 2.63 (m, 2H, CH₂), 1.22 (s, 3H, CH₃), 1.12 (s, 3H, CH₃) ppm; ¹³C NMR (126 MHz, DMSO-d₆) δ 157.0, 147.3, 140.0, 135.9, 128.5, 127.5, 126.9, 125.5, 121.4, 121.3, 119.4, 118.6, 107.0, 106.0, 70.2, 69.7, 69.4, 69.0, 53.9, 52.2, 51.6, 28.4, 25.7, 19.6 ppm; HRMS-ESI (*m/z*) calculated for C₃₁H₄₁N₃O₈ [M + H]⁺ 584.2972, found 584.2943 and [M + Na]⁺ 606.2791, found 606.2773.



HRMS-ESI spectrum of **SHL**



^1H NMR spectrum of **SHL** recorded in $\text{DMSO-}d_6$ at 500 MHz



^{13}C NMR spectrum of **SHL** recorded in $\text{DMSO-}d_6$ at 126 MHz

Supplemental Spectroscopic Experiments

1. General Information

Stock solutions of **SHL** (5 mM) were prepared in HPLC-grade acetonitrile. Stock solutions of metal ion salts (10 mM) were prepared in water and diluted in acetonitrile (1 mM). Salt solutions were prepared from dried perchlorate or chloride salts and these were used interchangeably.

For the selectivity studies, solutions were prepared (in triplicate) on the same microplate tray from 2 μL **SHL** and 2 μL of ion stock solutions, such that each replicate contained a 1:2 molar ratio of **SHL**: ion. 196 μL of HPLC grade acetonitrile was then added to dilute each replicate, such that the final concentrations of **SHL** and ions in each solution were 50 μM and 100 μM , respectively. The microplate tray was then incubated in the dark for 10 mins before reading. Absorbance and fluorescence spectra were recorded between 300-700 nm and 555-800 nm, respectively, at 25 °C using a BioTek Synergy H4 Hybrid Multi-Mode Microplate Reader scanning with a resolution of 5 nm. Fluorescence excitation was at 532 nm, with a bandgap of 9 nm and 100 gain setting. The assay tray was then removed and repetitive photoswitching was performed by exposure to 352 nm UV light from a filtered 8 W Hg lamp (UVP), or halogen white lamp for 10 min each with absorbance and fluorescence spectra obtained after each irradiation. The error bars presented represent a standard deviation about the mean value.

For the Job's Plot Analysis of Binding Stoichiometry, stock solutions of **SHL** (100 μM) and Li^+ salt (100 μM) were prepared separately in HPLC-grade acetonitrile. Solutions were prepared (in triplicate) in the same clear-bottom microplate tray from varying volumes of the **SHL** and Li^+ stock solutions until the total volume of each replicate was 200 μL , where each solution contained a constant total combined concentration of

$[\text{SHL}] + [\text{Li}^+] = 100 \mu\text{M}$. The microplate tray was then incubated in the dark for 10 mins before reading. Fluorescence emission spectra were recorded as described above. A Job's plot was derived by plotting the mean fluorescence at the maximum emission wavelength for each concentration ratio of ($[\text{SHL}]$, $[\text{Li}^+]$).

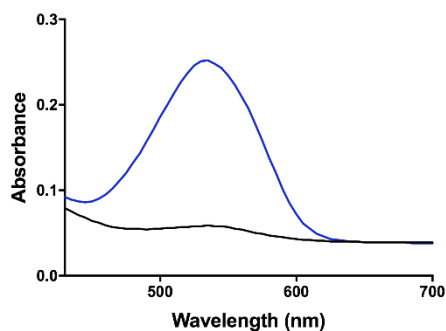


Figure S1. Absorbance spectra of **SHL** (50 μM) in the absence (black) and presence of Li^+ (blue, 100 μM).

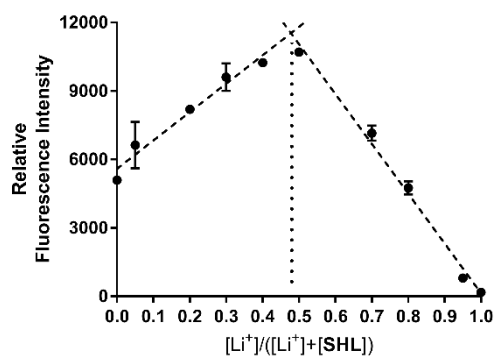


Figure S2. Job's plot analysis of binding stoichiometry of **SHL** with Li^+ . Maximum fluorescence at $X (= [\text{Li}^+]/([\text{Li}^+] + [\text{SHL}])) = 0.55$ depicted by vertical dotted line on the graph.

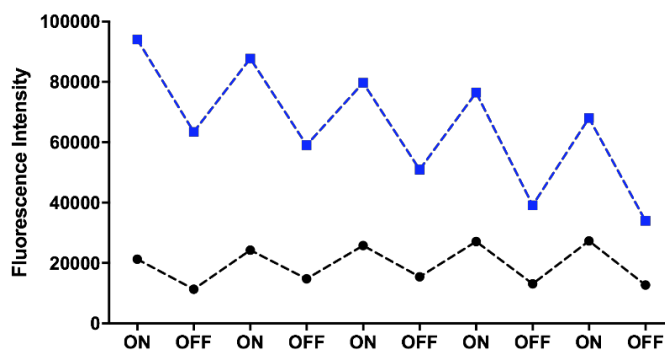


Figure S3. Photoswitching of **SHL** (50 μM) in the absence (black) and in the presence of Li^+ (100 μM , blue). Each “off-cycle” represents the fluorescence emission ($\lambda_{em} =$

approx. 635 nm) of the ring closed spiropyran without Li⁺ chelated. Each “on-cycle” represents the resultant fluorescence emission of ring-opened (**SHL**)MC-Li⁺.

2. Determination of Dissociation Constant (K_d) of **SHL**

Stock solutions of Li⁺ salt (0.02-2 mM) and **SHL** (5 mM) were prepared separately in HPLC-grade acetonitrile. Replicate solutions were prepared (in triplicate) in the same clear-bottom microplate tray and diluted in acetonitrile such that the final concentrations of **SHL** and Li⁺ in each solution were 50 μM and 1-100 μM, respectively. The microplate tray was then incubated in the dark for 10 mins before reading. Fluorescence emission spectra were recorded as described above. A concentration curve was prepared from the fluorescence emission maximum for each ion concentration. The apparent dissociation constant (K_d) of **SHL** for Li⁺ was then calculated by fitting an appropriate non-linear regression in GraphPad Prism version 7.02. The ‘Hill Plot with Specific Binding’ model was selected, as it represents a saturation binding experiment, where concentration of ‘radioligand’ (i.e. Li⁺) is varied and binding to the ‘receptor’ (i.e. merocyanine isomer of **SHL**) is measured, in this case as a fluorescence emission. The model uses the following equation,

$$Y = B_{max} * X^h / (K_d^h + X^h)$$

Where Y is the relative fluorescence intensity at any given concentration of metal ion, B_{max} is the maximum specific binding in the same units as Y (i.e. in this case the fluorescence at sensor saturation), X is the concentration of Li⁺ and K_d is the Li⁺ concentration needed to achieve the half-maximum binding at equilibrium, expressed in the same units as X. The parameter h is the Hill slope, and h = 1.0 when a monomer binds with no cooperativity to one site.

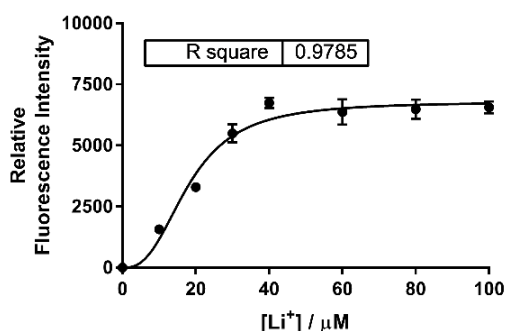


Figure S4. Metal ion titration curve of **SHL** (50 μM), in the presence of increasing concentrations of Li⁺ (1-100 μM). Each data point is measured from the sensor emission maxima. **SHL**-Li⁺ ($K_d = 18 \pm 2 \mu\text{M}$).

3. Determination of Quantum Yield (Φ) of **SHL**

A stock solution containing **SHL** (50 μM) and Li⁺ (100 μM) was prepared in HPLC-grade acetonitrile. Solutions were prepared (in triplicate) on the same clear-bottom microplate tray from varying volumes of the combined **SHL**/Li⁺ stock solution and HPLC-grade acetonitrile, until the volume of each replicate was 200 μL. The microplate tray was then incubated in the dark for 10 mins before reading. Absorbance (400-600 nm, 2 nm scanning resolution) and fluorescence emission spectra (535-800 nm, 5 nm scanning resolution, excitation 514 nm, 80 gain) were recorded at 25 °C using a BioTek Synergy H4 Plate Reader. These absorbance and fluorescence measurements was repeated for Rhodamine B (0, 1, 2, 3, 4, 5 μM), and a graph of integrated fluorescence vs absorbance at 514 nm (up to an approximate absorbance value of 0.1) was obtained. Quantum yield was calculated using the following equation:

$$\Phi_x = \Phi_{\text{ST}} (\text{Grad}_x/\text{Grad}_{\text{ST}})(\eta^2_x/\eta^2_{\text{ST}})$$

Where subscripts ST and X denote standard (Rhodamine B) and the unknown (**SHL**), respectively. Φ is fluorescence quantum yield, Grad is the gradient from the plot of integrated fluorescence intensity vs absorbance and η is the refractive index of the

solvent ($\eta_{(\text{water})} = 1.330$, $\eta_{(\text{acetonitrile})} = 1.344$). The fluorescence quantum yield of Rhodamine B in water at $\lambda_{\text{ex}} = 514 \text{ nm}$ is 0.31, as reported in the literature.³

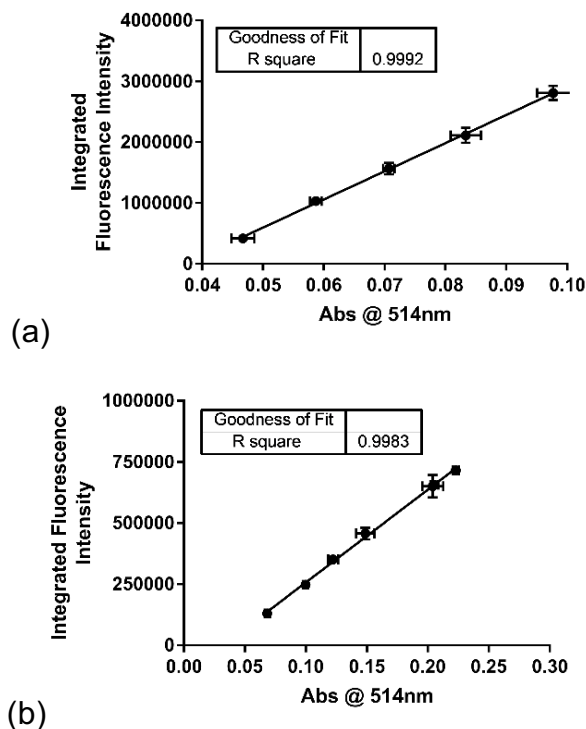


Figure S5. Integrated fluorescence spectra after excitation at 514 nm versus the absorbance at 514 nm for (a) Rhodamine B and (b) **SHL** -Li⁺ ($\Phi = 0.03$).

Supplemental Video

Time lapse recording of Li⁺ 'hot spots' for 300 s duration with 3 s interval. Li⁺ signal was increasing during the early stage of the video then dynamically turned on and off during the late stage of the video.